Investigating gas-phase defect formation in late-stage solidification using a novel phase-field crystal alloy model

Nan Wang, Nathan Smith, and Nikolas Provatas
Department of Physics, McGill University, Montreal, Québec, Canada H3A 2T8
(Received 11 May 2017; published 28 September 2017)

We study late-stage solidification and the associated formation of defects in alloy materials using a novel model based on the phase-field-crystal technique. It is shown that our model successfully captures several important physical phenomena that occur in the late stages of solidification, including solidification shrinkage, liquid cavitation and microsegregation, all in a single framework. By examining the interplay of solidification shrinkage and solute segregation, this model reveals that the formation of gas pore defects at the late stage of solidification can lead to nucleation of second phase solid particles due to solute enrichment in the eutectic liquid driven by gas-phase nucleation and growth. We also predict a modification of the Gulliver-Scheil equation in the presence of gas pockets in confined liquid pools.

DOI: 10.1103/PhysRevMaterials.1.043405

I. INTRODUCTION

Solidification of crystalline materials, particularly alloy materials, has been a topic of both theoretical and practical importance for many years [1,2]. Extensive works have been dedicated to understanding solidification patterns and resulting microstructures [3,4]. Near the end of solidification process, the volume fraction of solidified dendritic network reaches 90% or greater. This late stage solidification happens in highly confined interdendritic channels separated by solute-enriched liquid pools [2,4]. It has long been known that the solidification behavior at this late stage is associated with the formation of defects and second phase particles. Gas-phase defects, such as microporosity and hot tears in particular, form at this stage and are imprinted into the final solidified microstructure. However, our knowledge on late-stage solidification of low-concentration alloys is still very limited despite of its strong impact on final material properties [5].

In the classic picture of late-stage solidification, a partially solidified region with a small liquid volume fraction is called mushy zone and is typically seen as a semisolid [2]. Many experimental and theoretical studies have been dedicated to understand materials behavior in the mushy zone [6–11]. Since there is typically a density difference between the solid and the liquid melt, solidification in this confined environment has been known to generate local pressure changes due to shrinkage of the solid caused by density change. It has been shown in experiments that the pressure induced from solidification shrinkage may lead to porosity formation, hot tearing failure, deformation of the dendritic network and even recrystallization in solidified structure [12–15]. Niyama's criterion was developed to explain the formation of gas porosity [16]. Rappaz, Drezet, and Gremaud (RDG) developed a two-phase theory that takes into account both elastic and plastic deformation of the solid confinement in the formation of hot tears [17]. The nucleation of gas phase (or cavitation) in those continuum based models is typically determined by setting up a pressure threshold, which can be obtained from atomic level models [18,19].

Another important phenomenon that happens at the late stages of solidification is the precipitation of nonequilibrium or second phases [20]. Continuous enrichment of the confined liquid melts due to solute rejection at the solidification front (commonly known as microsegregation) leads to the formation of small secondary solid phases below the eutectic point [21–23]. Materials strength can be strongly affected by the size and distribution of those small particles [24,25]. Based on local solute partitioning, the Gulliver-Scheil equation has been widely used to explain the solute enrichment in eutectic liquid at the late stage. It is noteworthy that the solidification of secondary phases due to microsegregation and the formation of gas-phase defects (gas porosity and hot tears) have mainly been studied in separate contexts in most previous works despite of the fact that they can be coupled at the small length scales involved during the late stages of solidification.

While the classic solidification theory has been very successful in predicting microstructures on the order of microns and above, its fundamental length scale is tied to the Mullins-Sekerka instability wavelength [1]. Since the initial size of the confined interdendritic channels and isolated liquid pools is usually associated with the primary and the secondary dendrite arm spacing, which are manifestations of the Mullins-Sekerka instability wavelength, the most relevant length scale in the late stages of solidification is likely to be smaller than the length scale of classic solidification theory. On the other end, when the liquid channels are narrowed down to the size that is comparable to the solid-liquid interface width (on the order of 1 nm), theories based on interface disjoining potentials have been developed recently to explain coalescence and bridging of grains during the last stages of solidification [5,26]. A comprehensive understanding of the solidification behavior that occurs in a confined environment on the size of 10 nm up to a few microns is still largely missing.

To investigate late-stage solidification in confined volumes and its associated phenomena involving gas-phase defect formation and secondary solid phase formation, one requires a model that is capable of capturing solute segregation, solidification shrinkage, gas-phase nucleation, elastic and potential plastic deformation in the solid under confinement [27]. This seemingly daunting task has been made possible by recent progress in the phase-field-crystal (PFC) methodology [28,29]. Originally developed for solidification problems in pure materials, the PFC model naturally incorporates elasticity and lattice defects (dislocations and grain boundaries) in solid

 ©2017 American Physical Society

state [30]. Later works extended this modeling technique to alloy materials [31], solid-state structural transformation [32–34], and gas-phase nucleation [35]. Typical length scale of PFC model is about 10–100 nm, which coincides with what is required to investigate late-stage solidification process. This method has been also used to study dendritic crystal growth, which is the dominant form of solidification at low solid volume fraction [29], and the effect of disjoining potential in grain coalescence which is the very last stage of solidification [36]. Studies of late-stage solidification using microscopic continuum techniques have been lacking. Specifically, here have been no systematic PFC studies of density change in solidification, and until recently there were no PFC models developed to incorporate gas-phase formation during solidification. Moreover, traditional phase-field solidification models typically preclude both these effects explicitly.

In this work, we formulate a novel PFC model that naturally and self-consistently incorporates both solidification shrinkage and gas phase nucleation, alongside the usual elasto-plastic effects that the PFC paradigm is well known for. It is shown that shrinkage induced pressure in the liquid near the solidification front is reproduced. By considering gas-phase formation, it is shown that the late-stage Gulliver-Scheil (GS) type microsegregation behavior in the liquid can be modified. As a result, we also demonstrate that the formation of gas porosity can facilitate the nucleation and growth of second phase particles in enriched liquid pools.

II. MODEL FORMULATION

A. Free energy functional

The PFC model developed for this work is a synthesis of previous alloy and gas-phase models [31,34,35]. The dimensionless free energy functional is formulated in terms of a concentration filed $c(\mathbf{r})$ and dimensionless PFC density field $n(\mathbf{r})=(\rho-\bar{\rho})/\bar{\rho}$, where $\bar{\rho}$ is the reference fluid density around which the free energy is expanded. Its form is

$$F_{\mathrm{PFC}} = F_{\mathrm{ideal}} + F_{\mathrm{pair}} + F_{MP}, \tag{1}$$

where the expanded ideal part is given by

$$F_{\mathrm{ideal}} = \int \left[\epsilon\frac{n(\mathbf{r})^2}{2} - W_1\frac{n(\mathbf{r})^3}{6} + W_2\frac{n(\mathbf{r})^4}{12}\right]d\mathbf{r}, \tag{2}$$

and ϵ, W_1, and W_2 are constants (defined below). The spatial coordinate is scaled by the solid phase lattice constant. The pair correlations terms are

$$F_{\mathrm{pair}} = F_{nn} + F_{nc} + F_{cc}, \tag{3}$$

where F_{nn} denotes density correlations, F_{cc} correlations in concentration, and F_{nc} density-concentration correlations. The above pair correlation contributions are written as in Ref. [34]

$$F_{nn} = \int n(\mathbf{r}_1)\left\{\int [\xi(c)C^{AA}(\mathbf{r}_1-\mathbf{r}_2) + \xi(1-c)C^{BB}(\mathbf{r}_1-\mathbf{r}_2)]n(\mathbf{r}_2)d\mathbf{r}_2\right\}d\mathbf{r}_1, \tag{4}$$

$$F_{nc} = \int \zeta(c(\mathbf{r}_1))\,n(\mathbf{r}_1)\left[\int \chi_c(\mathbf{r}_1-\mathbf{r}_2)\,\zeta(c(\mathbf{r}_2))\,n(\mathbf{r}_2)\,d\mathbf{r}_2\right]d\mathbf{r}_1, \tag{5}$$

and

$$F_{cc} = \int \alpha|\nabla c|^2 d\mathbf{r}., \tag{6}$$

where α is a constant. The contribution from multipoint correlations is [35]

$$F_{MP} = \sum_{m=3}^{4}\frac{1}{m}\int d\mathbf{r}_1...d\mathbf{r}_m\chi_m(\mathbf{r}_1,...,\mathbf{r}_m)n(\mathbf{r}_1)...n(\mathbf{r}_m). \tag{7}$$

For the density pair correlation functions in Eq. (4), we consider single peak approximations, i.e., $C^{AA} = B_{x1}(q_1^2+\nabla^2)^2$ and $C^{BB} = B_{x2}(q_2^2+\nabla^2)^2$, with q_1 and q_2 being the first peak positions of the $c=0$ and $c=1$ structures, respectively, in reciprocal space. Solid phase lattice parameter a is given by $a=4\pi/(\sqrt{3}q_1)$. The function ξ is smooth and interpolates between crystal structures depending on local concentration as in Ref. [34]. Assuming the concentration field c changes slowly on the scale of the atomically varying density n, Eq. (5) is approximated by replacing $c(\mathbf{r}_2)$ with $c(\mathbf{r}_1)$ and choosing $|\zeta(c)|^2 = \frac{u_1}{2}(c-c_0)^2 + \frac{v_1}{4}(c-c_0)^4$. The density-concentration pair correlation is approximated by $\chi_c(\mathbf{k}) = e^{-\frac{\mathbf{k}^2}{2\lambda_c}}$ in reciprocal space. The multipoint density correlations are chosen as in Ref. [35] to be $\chi_3 = (a_1\epsilon+b_1)\chi(\mathbf{r}_1-\mathbf{r}_2)\chi(\mathbf{r}_1-\mathbf{r}_3)$ and $\chi_4 = c_1\chi(\mathbf{r}_1-\mathbf{r}_2)\chi(\mathbf{r}_1-\mathbf{r}_3)\chi(\mathbf{r}_1-\mathbf{r}_4)$, with $\chi(\mathbf{k}) = e^{-\frac{\mathbf{k}^2}{2\lambda}}$ in reciprocal space. The parameters λ_c, λ, a_1, b_1, and c_1 are constants used to set the thermodynamic properties of the alloy system.

B. Thermodynamic properties

Some basic thermodynamic properties of our PFC model with the parameters used in this work are shown in Fig. 1. Model parameter ϵ serves as a model temperature parameter of our PFC model [30], while in Fig. 1, c and n_o refer to the mean concentration and mean density, respectively. Figure 1(a) is a typical eutectic phase diagram of a binary alloy. Figure 1(b) shows that the uniform phase in this model may have a coexistence region (the solid line) of a high density phase (liquid phase) and a low density phase (vapor phase) depending on model parameter ϵ. Figures 1(c) and 1(d) show the density change associated with solidification in the α-liquid and β-liquid coexistence region. It is noted that cavitation can occur in one of two ways. One is a localized transition of liquid (or solid) to vapour, leading to a gas-phase pocket. The second is dissolved gas content. The demonstrated cavitation thermodynamics in Fig. 1(b) can be adjusted to account for dissolved gas content by changing the initial conditions and density of the liquid to correspond to different dissolved gas fractions. However, the current model does not incorporate such dissolved gas concentration explicitly.

C. Dynamics

Dynamical evolution of n and c follow conserved variational dynamics given by

$$\frac{\partial n}{\partial t} = \nabla\cdot\left(M_n\nabla\frac{\delta F}{\delta n}\right) + \eta, \tag{8}$$

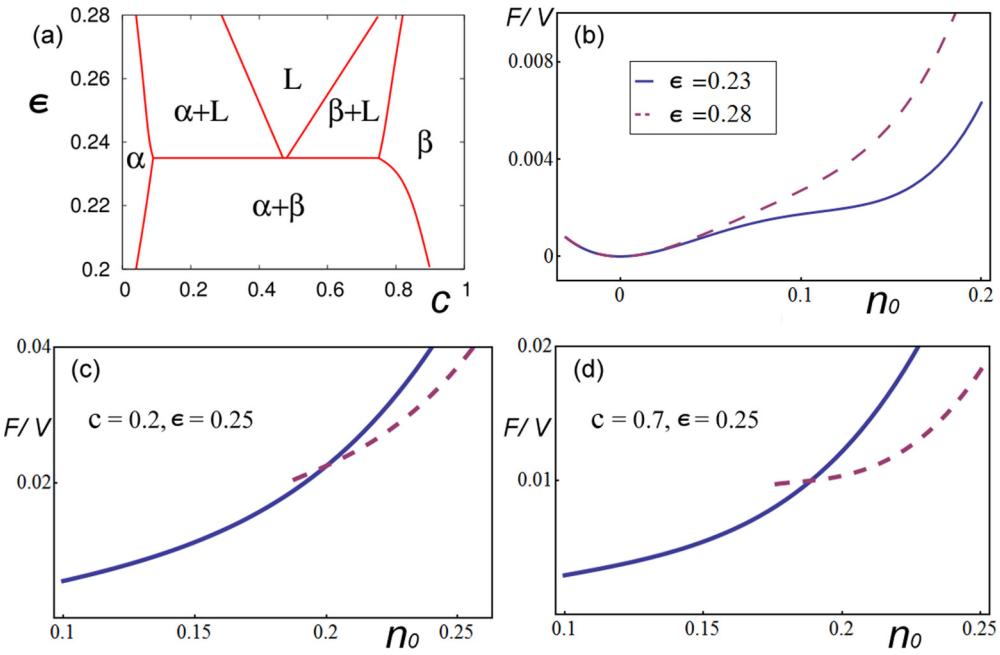

FIG. 1. Basic thermodynamic properties of PFC model. Here c and n_o refer to mean concentration and mean density, respectively. (a) Numerical phase diagram showing two solid phases α and β and a liquid phase L. (b) Demonstration of liquid→ liquid-vapour transition in eutectic liquid ($c = 0.5$) with temperature (ϵ). This transition in a liquid is a path to cavitation of the liquid. (c) and (d) Demonstration of α-liquid (c) and β-liquid (d) coexistence region at a given concentration, where solid and liquid state free energies are shown with dashed and solid lines, respectively. Model parameters used in this work are $W_1 = 1.3$, $W_2 = 0.6$, $\alpha = 8.0$, $B_{x1} = 0.3$, $B_{x2} = 0.9$, $q_1 = \sqrt{2}$, $q_2 = 1$, $u_1 = 6.0$, $v_1 = 3.0$, $c_0 = 0.5$, $a_1 = 43$, $b_1 = -30$, $c_1 = 90$, and $\lambda = \lambda_c = 0.04$.

for density field and

$$(1+\bar{n})\frac{\partial c}{\partial t} = \nabla\cdot\left[(1+\bar{n})M_c\nabla\frac{\delta F}{\delta c}\right], \tag{9}$$

for the concentration field, with corresponding mobility M_n and M_c. Here, $\bar{n}(r) = \int n(r')\chi(r-r')dr'$ is the locally averaged spatial density and the stochastic noise η satisfies the fluctuation-dissipation theorem $\langle\eta(\mathbf{r},t),\eta(\mathbf{r}',t')\rangle = -2(M_n/\bar{\rho}a^d)\nabla^2\delta(\mathbf{r}-\mathbf{r}')\delta(t-t')$, where $\bar{\rho}$ is the reference density about which the PFC model is expanded. Equation (9) approximates c dynamics by weighting changes in solute concentration and flux by the local average density since c is not in general a conserved field. This generalized concentration dynamics for spatially inhomogeneous $\bar{n}$ is reduced to the classic concentration dynamics when $\bar{n}$ is assumed to be constant in the system as in previous PFC literature. It has been shown that nucleation related critical fluctuations are essentially on the interface length scale, therefore we only included a noise term in the atomically resolved order parameter field and ignored fluctuations in the slow varying concentration field.

III. RESULTS AND DISCUSSIONS

A. Shrinkage pressure

An important phenomenon that arises at the late stage of solidification is a pressure drop in a liquid pool confined by a surrounding solid network. Since solidification shrinkage happens at the solid-liquid interface, the local mass shortage at the interface needs to be fed through liquid transport. Under sharp interface conditions, this mass balance leads to a liquid velocity normal to the solidification front given by $v_{ln} = \bar{\beta}v_n$, where v_n is the velocity of the solid-liquid front and $\bar{\beta} = (\rho_S - \rho_L)/\rho_L$ is the shrinkage factor [2], where ρ_S is the solid density and ρ_L is the liquid density. Assuming liquid flow in the small confined geometry is driven only by a pressure gradient (Darcy's law), the pressure drop in the liquid at distance d from a large liquid reservoir is described by an effective 1D equation $\triangle P(d) = \bar{\beta}v_n\int_0^d g(x)dx$ where $g(x) = \mu f_l(x)/K(x)$, with μ the liquid viscosity, K the mushy zone permeability, and f_l the local liquid volume fraction. The boundary condition $f_l(0) = f_l^D$ where f_l^D the upper limit of the liquid fraction from which the Darcy type flow becomes dominant. This is a quasi-one-dimensional model where the effective material properties perpendicular to the interface normal enters in the liquid fraction f_l. It has also been extended to incorporate elastic and plastic deformations due to solid confinement [17]. It considers fluid flow due to density change caused by shrinkage. While the PFC model does not allow for fluid flow, we expect that it qualitatively captures pressure change effects due to shrinkage in a narrow channel.

We examined shrinkage-induced pressure drop for solidification in a typical geometry shown in the inset of Fig. 2 using the PFC model formulated in Eqs. (1)–(9). Simulations are performed in a 4096 by 512 grid box with grid spacing $\Delta x = \sqrt{3}\pi/(8q_1)$ and $\Delta y = \pi/(4q_1)$. Pressure in the liquid is measured along the center line shown in the inset of Fig. 2. The main part of Fig. 2 shows the model's predicted shrinkage-induced pressure drop through the liquid channel. This maximum pressure change is found to

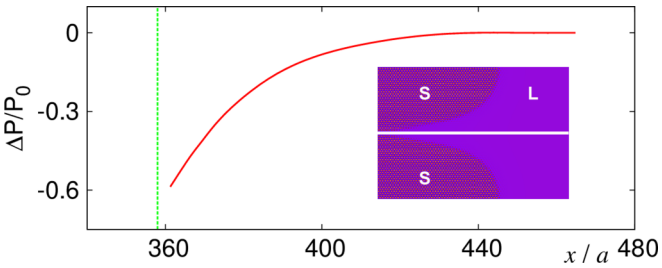

FIG. 2. Pressure drop in liquid due to solidification shrinkage. Pressure change is plotted along the horizontal line shown in the inset as a function of position (x) in the liquid. x/a measures the distance from reference liquid reservoir. The green vertical dashed line indicates the position where $f_l = 0$. In the inset, S refers to solid and L to liquid. Numerical dimensions are given in the text. Other model parameters are given in Fig. 1.

depend on both shrinkage factor β and solid interface velocity v_n in the simulation. This behavior is shown in Fig. 3. It is noted that the relation between pressure drop and solidification velocity (or shrinkage factor) in Fig. 3 is monotonic but not necessarily linear as predicted by the classic

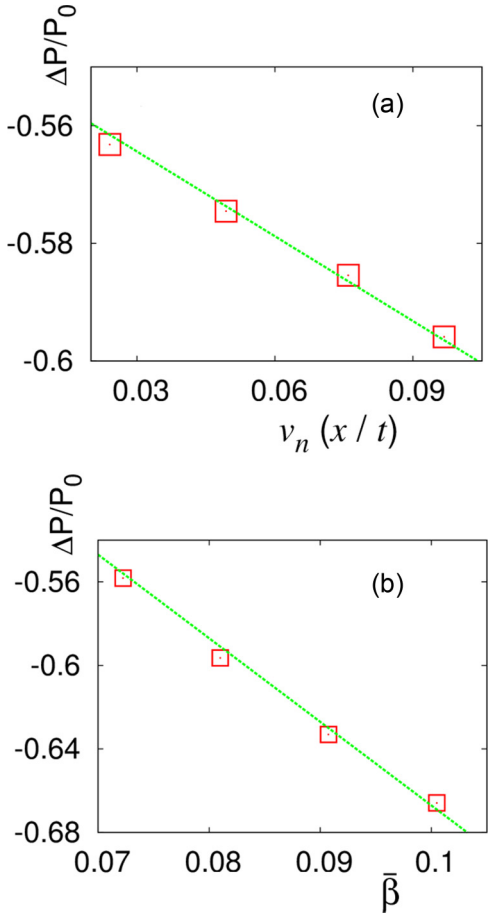

FIG. 3. (a) Peak pressure drop ahead of the interface as a function of solidification velocity. (b) Pressure drop as a function of shrinkage factor $\bar{\beta}$. P_0 is the liquid pressure far from the solid. The green dashed lines are to guide the eye. Model parameters are given in Fig. 2.

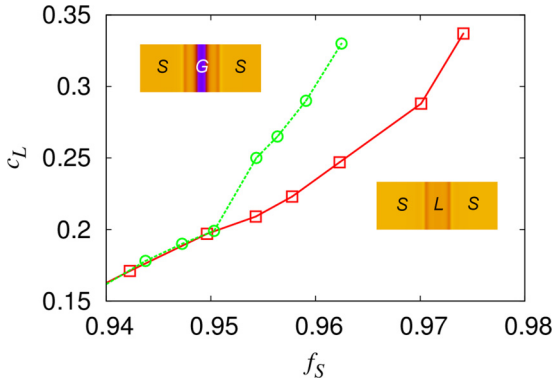

FIG. 4. Solute segregation in eutectic liquid channel with (red curve) and without (green curve) gas-phase formation in late-stage solidification. The top left inset figure corresponds to the top (green) data. The bottom right inset figure corresponds to the bottom (red) data. The color fields in the inset figures show the density configuration of the system corresponding to the highest concentration of of each curve. Solid phase has the highest density and is colored as bright yellow. Gas phase has the lowest density and is colored as dark blue. Liquid is colored as dark yellow. Solid, liquid, and gas phases are labeled using letters S, L, G, respectively. The simulations start with $f_L = 0.06$, $c_L = 0.15$ and liquid density $\rho_L/\rho_S = 1.0$ for the bottom line, $\rho_L/\rho_S = 0.85$ for the top line. Cooling rate $\epsilon/t = 10^{-6}$. Solute concentration is averaged over the liquid.

shrinkage model discussed above, which considers only pure materials and fluid flow.

B. Segregation and gas-phase nucleation

Microsegregation of solute atoms into the last eutectic liquid is another important phenomenon that could strongly affect the properties of final solid since it is related to precipitation of second phase particles. To increase the solid volume fraction by df_s, the solidification process has to reject solute $(c_l - c_s)df_s$ with local liquid concentration c_l and solid concentration c_s. The remaining liquid is then enriched due to this rejected solute by $dc_l = (c_l - c_s)df_s/f_l$ assuming it is evenly redistributed within the liquid. With $f_s + f_l = 1$, partition coefficient $k = c_s/c_l$ and boundary condition $c_l = c_0$ at $f_s = 0$, the averaged concentration segregation c_L can be expressed as a function of the final solid fraction f_S,

$$c_L = c_0(1 - f_S)^{k-1}, \tag{10}$$

which is commonly known as the Gulliver-Scheil equation [2]. It has been widely used to explain the formation of high concentration nonequilibrium phases at the late stage of solidification. However, Eq. (10) does not take into account the effect of liquid pressure drop and gas phase nucleation (cavitation), which can also happen at late-stage solidification (or high solid volume fraction). A modification of Eq. (10) that considers a gas-phase fraction f_g can be written as

$$\int_{c_L^*}^{c_L} \frac{dc_l}{c_l} = (1-k)\int_{f_S^*}^{f_S} \frac{1}{1 - f_s - f_g} df_s, \tag{11}$$

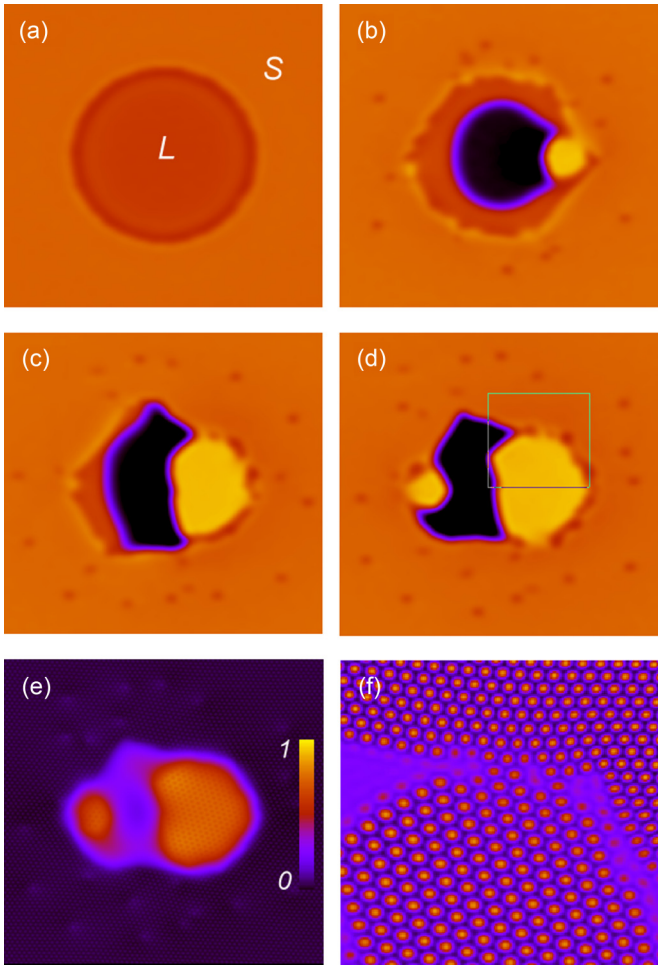

FIG. 5. Liquid cavitation promoting the nucleation and growth of the high concentration solid phase. (a)–(d) are average density maps. (a) Liquid pool confined in a low concentration solid α phase. The solid and the liquid regions are marked by S and L, respectively. (b) Cavitation of the liquid triggers the nucleation of the high concentration solid β phase. (c) Subsequent growth of the high concentration β solid and associated deformation of the remaining gas pocket. (d) A second nucleation event occurs to the left of the gas pocket toward the end of the simulation sequence. (e) Solute concentration map of (d). The color bar to the right shows the concentration scale. (f) Microscopic PFC order parameter (density) field showing different solid structures for the triple-phase region in the inset box of frame (d). Small dark dots in the solid seen in (b)–(d) are dislocations formed during solidification. The starting configuration is a separate liquid pool of size $R = 30a$ with $\rho_L/\rho_S = 0.85$, $c_L = 0.3$, and $c_S = 0.07$. The system is quenched below eutectic point ($\epsilon = 0.2$)

where c_L^* and f_S^* are corresponding liquid concentration and solid fraction before gas-phase nucleation. Since the rejected solute has to be distributed within a smaller liquid volume, Eq. (11) predicts a potentially higher liquid concentration for the same solid volume fraction at the late stage of solidification. Numerical results using our PFC model predict precisely such a behavior. We simulated solidification of a nanoscale liquid channel enclosed by two solid slabs for two cases, one where the channel remains liquid and the other where the liquid film partially transforms into gas phase. As shown in Fig. 4, the case where liquid cavitation occurs leads to a higher concentration of the surrounding liquid. The simulation in Fig. 4 is performed in a 16384 by 16 grid where only one unit cell is contained in the y direction. It is noted that the nucleation of gas phase demonstrated here is primarily due to change of pressure and is relatively insensitive to solute concentration. To our knowledge, this is the first time this modified GS type mechanism is proposed by a computational model. Such a relation may lead to interesting phenomena, one of which is demonstrated in the next section.

C. Coupled nucleation of gas-phase defects and second phase formation

The interplay of segregation and gas-phase nucleation demonstrated in Fig. 4 should be most significant in deeply quenched liquid since the fast solidification rate is more likely to generate large pressure drop that leads to cavitation. A relevant two-dimensional scenario wherein a small confined liquid pool is quenched below the eutectic point was investigated using our PFC model. The results are shown in Fig. 5 and reveal an interesting phenomenon where the pressure change leading to liquid cavitation promotes the nucleation and growth of the second phase solid, in this case β phase. Details of this phenomenon are described in the figure caption. Another interesting phenomenon that we found accompanies this process is the growth and subsequent migration of dislocations near the solid liquid interface. We will study the source and migration of these defects during solidification in a future study as it goes beyond the scope of this paper, which aims to introduce a new modeling tool for materials processes. To our knowledge, this mechanism of second phase solid nucleation facilitated by gas-phase formation has not been previously reported in literature.

IV. CONCLUSION

In summary, by incorporating density differences in a multiphase alloy system, a novel PFC model is developed to investigate defect formation in the late stages of rapid solidification. It is shown that this formalism is capable of capturing the physics of solidification shrinkage, gas-phase nucleation, microsegregation, elastic and plastic deformation, all of which are relavent to late-stage solidification. We revealed, for the first time to our knowledge, an interesting interplay of microsegregation and gas phase nucleation at the late stage of solidification that can lead to second-phase solid formation near gas-phase defects. Although the noise-induced nucleation mechanism is only qualitatively incorporated in the current model, it is not crucial to the main results presented here, and we fully expect these to also occur under a more realistic form PFC noise added to the dynamical equations. In this work, since both the modified GS relation in Fig. 4 and the second solid nucleation in Fig. 5 are only affected by gas-phase fraction and pressure change, the nucleation of the second phase solid is qualitatively expected to occur due

to enhanced solute enrichment. The PFC model developed in this work is expected to be easily generalized to study the combined effect of segregation and defect nucleation in other multiphase systems.

ACKNOWLEDGMENTS

We thank The National Science and Engineering Research Council of Canada and the Canada Research Chairs Program for funding, and Compute Canada for HPC resources.

[1] J. S. Langer, Rev. Mod. Phys. **52**, 1 (1980).
[2] J. A. Dantzig and M. Rappaz, *Solidification* (EPFL Press, Lausanne, 2009).
[3] W. J. Boettinger, J. A. Warren, C. Beckermann, and A. Karma, Annu. Rev. Mater. Res. **32**, 163 (2002).
[4] M. Asta, C. Beckermann, A. Karma, W. Kurz, R. Napolitano, M. Plapp, G. Purdy, M. Rappaz, and R. Trivedi, Acta Mater. **57**, 941 (2009).
[5] M. Rappaz, A. Jacot, and W. J. Boettinger, Metall. Mater. Trans. A **34**, 467 (2003).
[6] D. J. Rowenhorst, J. P. Kuang, K. Thornton, and P. W. Voorhees, Acta Mater. **54**, 2027 (2006).
[7] N. D. Souza, H. B. Dong, M. G. Ardakani, and B. A. Shollock, Scr. Mater. **53**, 729 (2005).
[8] A. Heckl, R. Rettig, S. Cenanovic, M. Göken, and R. F. Singer, J. Cryst. Growth **312**, 2137 (2010).
[9] M. Sistaninia, A. B. Phillion, J. M. Drezet, and M. Rappaz, Acta Mater. **60**, 3902 (2012).
[10] D. Montiel, S. Gurevich, N. Ofori-Opoku, and N. Provatas, Acta Mater. **77**, 183 (2014).
[11] M. Zhu, L. Zhang, H. Zhao, and D. M. Stefanescu, Acta Mater. **84**, 413 (2015).
[12] A. K. Dahle, D. H. St. John, H. J. Thevik, and L. Arnburg, Metall. Mater. Trans. B **30**, 287 (1999).
[13] H. Wang, F. Liu, and G. Yang, J. Mater. Res. **25**, 1963 (2010).
[14] Y. Li, D. Qian, J. Xue, J. Wan, A. Zhang, N. Tamura, Z. Song, and K. Chen, Appl. Phys. Lett. **107**, 181902 (2015).
[15] S. Wildeman, S. Sterl, C. Sun, and D. Lohse, Phys. Rev. Lett. **118**, 084101 (2017).
[16] E. Niyama, T. Uchida, M. Morikawa, and S. Saito, AFS Int. Cast Metals Res. J. **7**, 52 (1982).
[17] M. Rappaz, J. M. Drezet, and M. Gremaud, Metall. Mater. Trans. A **30**, 449 (1999).
[18] J. B. Adams and W. G. Wolfer, Acta Metall. Mater. **41**, 2625 (1993).
[19] Y. Cai, H. A. Wu, and S. N. Luo, J. Chem. Phys. **140**, 214317 (2014).
[20] W. Kurz and R. Trivedi, Metall. Trans. A **22**, 3051 (1991).
[21] A. Latz, S. Sindermann, L. Brendel, G. Dumpich, F.-J. Meyer zu Heringdorf, and D. E. Wolf, Phys. Rev. B **85**, 035449 (2012).
[22] D. Tourret and Ch.-A. Gandin, Acta Mater. **57**, 2066 (2009).
[23] O. Shuleshova, D. Holland-Moritz, W. Löser, G. Reinhart, G. N. Iles, and B. Büchner, Europhys. Lett. **86**, 36002 (2009).
[24] E. Nes, N. Ryum, and O. Hunderi, Acta Metall. **33**, 11 (1985).
[25] N. Wang, Y. H. Wen, and L. Q. Chen, Comput. Mater. Sci. **93**, 81 (2014).
[26] N. Wang, R. Spatschek, and A. Karma, Phys. Rev. E **81**, 051601 (2010).
[27] D. M. Stefanescu, Int. J. CastMetals Res. **18**, 129 (2005).
[28] N. Provatas and K. Elder, *Phase-Field Methods in Material Science and Engineering* (Wiley, Weinheim, 2010).
[29] H. Emmerich, H. Löwen, R. Wittkowski, T. Gruhn, G. I. Tóth, G. Tegze, and L. Gránásy, Adv. Phys. **61**, 665 (2012).
[30] K. R. Elder and M. Grant, Phys. Rev. E **70**, 051605 (2004).
[31] K. R. Elder, N. Provatas, J. Berry, P. Stefanovic, and M. Grant, Phys. Rev. B **75**, 064107 (2007).
[32] M. Greenwood, N. Provatas, and J. Rottler, Phys. Rev. Lett. **105**, 045702 (2010).
[33] K.-A. Wu, M. Plapp, and P. W. Voorhees, J. Phys.: Condens. Matter **22**, 364102 (2010).
[34] M. Greenwood, N. Ofori-Opoku, J. Rottler, and N. Provatas, Phys. Rev. B **84**, 064104 (2011).
[35] G. Kocher and N. Provatas, Phys. Rev. Lett. **114**, 155501 (2015).
[36] J. Mellenthin, A. Karma, and M. Plapp, Phys. Rev. B **78**, 184110 (2008).